

Dual-domain Modulation Network for Lightweight Image Super-Resolution

Wenjie Li, Heng Guo, Yuefeng Hou, Guangwei Gao, and Zhanyu Ma

Abstract—Lightweight image super-resolution (SR) aims to reconstruct high-resolution images from low-resolution images with limited computational costs. We find existing frequency-based SR methods cannot balance the reconstruction of overall structures and high-frequency parts. Meanwhile, these methods are inefficient for handling frequency features and unsuitable for lightweight SR. In this paper, we show introducing both wavelet and Fourier information allows our model to consider both high-frequency features and overall SR structure reconstruction while reducing costs. Specifically, we propose a dual-domain modulation network that utilize wavelet-domain modulation self-Transformer (WMT) plus Fourier supervision to modulate frequency features in addition to spatial domain modulation. Compared to existing frequency-based SR modules, our WMT is more suitable for frequency learning in lightweight SR. Experimental results show that our method achieves a comparable PSNR of SRFormer [1] and MambaIR [2] while with less than 50% and 60% of their FLOPs and achieving inference speeds 15.4x and 5.4x faster, respectively, demonstrating the effectiveness of our method on SR quality and lightweight. Codes will be released upon acceptance.

Index Terms—Lightweight super-resolution, Dual-domain, Fourier domain, Wavelet domain, Transformer

I. INTRODUCTION

IMAGE super-resolution (SR) aims at reconstructing high-resolution (HR) images from low-resolution (LR) images. Most SR methods [3], [4] require high computational costs, limiting their application in devices with limited resources. As shown in Fig. 1, this paper focuses on the lightweight SR task, aiming to improve existing SR performance while reducing model size and accelerating inference.

Existing lightweight SR methods [5]–[7] only focus on the *spatial domain*, *i.e.*, spatial domain reconstruction and spatial domain supervision, resulting in a limited range of pixels utilized for inference as shown in the second column of Fig. 2, where LAM [8] indicate use a broader range of pixels in inference are favorable to improve SR. To utilize more pixels, they typically stack many blocks, which is computationally inefficient. For example, SwinIR-light [5] and SRFormer-light [1] have nearly 900K parameters and more than 1.3 seconds of inference speed at the scale of $\times 2$, respectively. Therefore, lightweight SR still remains an open problem.

Wenjie Li, Heng Guo, and Zhanyu Ma are with the Pattern Recognition and Intelligent System Laboratory, School of Artificial Intelligence, Beijing University of Posts and Telecommunications (BUPT), Beijing 100080, China (e-mail: {cswjli, guoheng, mazhanyu}@bupt.edu.cn).

Yuefeng Hou is with the School of Microelectronics, Tianjin University (TJU), Tianjin 300072, China (e-mail: houyuefeng@tju.edu.cn).

Guangwei Gao is with the Institute of Advanced Technology, Nanjing University of Posts and Telecommunications (NJUPT), Nanjing 210046, China (e-mail: csggao@gmail.com).

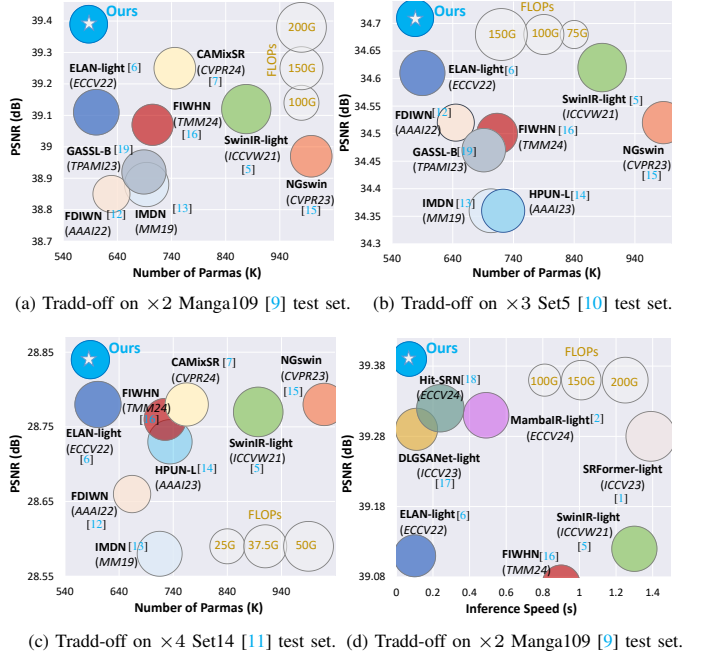


Figure 1: Efficiency trade-offs between our method and existing methods. Our method achieves a better balance in terms of PSNR, model size, and inference speed than existing methods.

In this paper, we handle the lightweight SR with the spatial and *frequency domain* reconstruction. Our insight comes from recent SR methods [20]–[23] that expand the range of pixel utilization with additional frequency information, typically in the Fourier or wavelet domains, to improve SR performance. However, as shown in the third to fifth columns of Fig. 2, compared to spatial-based methods, though these methods expand the range of pixel utilization with fewer params, we also observe these methods face challenges in balancing high-frequency textures and overall structures (PSNR/SSIM). Specifically, Fourier domain-based methods [20], [21], [24], [25] help regulate the global frequency distribution, optimizing the overall structure and leading to high PSNR values. However, it fails to effectively emphasize high-frequency features, which results in blurred high-frequency textures. Wavelet domain-based methods [22], [23] facilitate to emphasize on high-frequency features of images, resulting in clear high-frequency textures. However, the inconsistency of different frequency subbands in the direction of gradient descent is large and unfavorable for controlling losses, thus limiting overall structures.

To leverage frequency analysis for lightweight SR and address the challenge of balancing high-frequency textures and

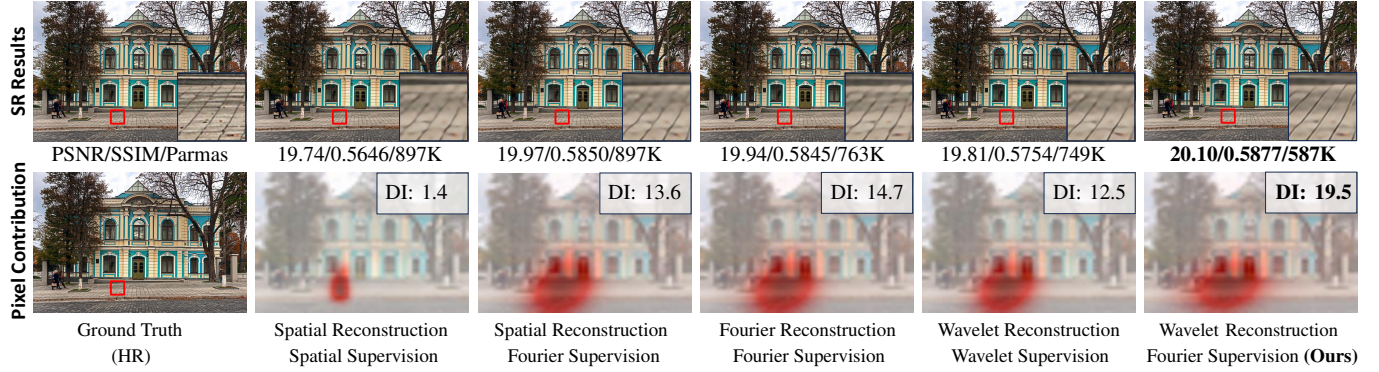


Figure 2: By reconstructing features in the wavelet domain and supervising the process in the Fourier domain, our method recovers precise textures and achieves the highest PSNR. Meanwhile, compared to existing methods [20], [22], [24] that use frequency information to expand pixel utilization, our method achieves a higher DI score, which quantifies the pixel contribution area, demonstrating its ability to capture more necessary pixel range for reconstruction.

overall structures, we reconstruct features in the wavelet domain and apply supervision in the Fourier domain. Specifically, wavelet transforms effectively decompose high- and low-frequency subbands, facilitating the modeling of their relationships, while Fourier supervision provides an efficient means to regulate the global frequency distribution. As shown in the sixth column of Fig. 2, compared to existing frequency-based methods, our method expands the range of pixel utilization (see DI score) while avoiding blurred high-frequency textures or inaccurate overall structures with the least params.

Based on the observations above, we propose a Dual-domain Modulation Network (DMNet) for lightweight SR. Our DMNet contains two modules: Wavelet-domain Modulation Transformer (WMT) and Spatial-domain Modulation Transformer (SMT), which modulate the wavelet and spatial domain information separately, which utilize self-attention to separately capture the correlations among different wavelet frequency and spatial domain features. Meanwhile, we separately utilize Fourier loss and image reconstruction loss to supervise frequency and spatial domain reconstruction. Our design ensures the overall similarity of SR images with ground truth while highlighting high-frequency features absent in LR images. Additionally, WMT combines self-attention and dynamic convolution to extract wavelet-domain features, capturing long-range dependencies and adapting to various frequency components, enabling efficient processing of frequency-domain features. As depicted in Fig. 1 (a), (b), and (c), our method achieves the highest PSNR with fewer Params and FLOPs compared to existing lightweight SR methods. Moreover, as shown in Fig. 1 (d), our method delivers the highest PSNR with minimal FLOPs and the fastest inference speed compared to recent lightweight Transformer- and Mamba-based methods.

In summary, the contributions of this paper are as follows:

- We find hybrid frequency domain utilization, combining wavelet features with Fourier supervision, effectively balances overall structure and high-frequency reconstruction.
- We propose a WMT based on wavelet transform, which can highlight the relationship between high- and low-frequency contents, further improving SR texture accuracy.

Table I: Comparison of our method with existing frequency-based SR methods, where CNN or Transformer structure refers to the structure when utilizing frequency domain information. Our method incorporates the advantages of hybrid frequency domain and presents a new frequency-based Transformer module that suitable for lightweight SR.

Frequency Type	CNN Structure	Transformer Structure
Fourier domain (Blur textures)	SFMNet [26], FDSR [27], etc	FSAS [24], SFANet [28], etc
Wavelet domain (Poor PSNR)	JWSGN [22], WFEN [29], etc	FSR [23], SODA-SR [30], etc
Wavelet+Fourier	-	Ours (Clear textures and high PSNR)

- Extensive experiments demonstrate that our DMNet can outperform existing lightweight SR methods in synthetic and real datasets with fewer Params and FLOPs.

II. RELATED WORK

This paper aims to utilize frequency information for lightweight SR. In the following, we briefly summarize recent works on lightweight SR and frequency-based SR, respectively.

A. Lightweight SR Methods

To promote realistic adoption, lightweight SR [31] has grown significantly. FSRCNN [32] enhances pre-sampling to reduce computational costs. CARN [33] incorporates a recursive mechanism to conserve module parameters. IMDN [13] introduces multilevel feature distillation to enhance models. DDistill-SR [34] incorporates reparameterization on top of information distillation to further improve efficiency. DRSAN [35] leverages dynamic residual attention to limit complexity by adaptively adjusting its structure based on input statistics. FDIWN [12] and FIWHN [16] improve efficiency by mitigating the activation function's negative impact. To extract long-range features, SwinIR [5] introduces window-based Transformers to learn globally to address the demand for long-range modeling features. ELAN [6] accelerates the model by sharing weights

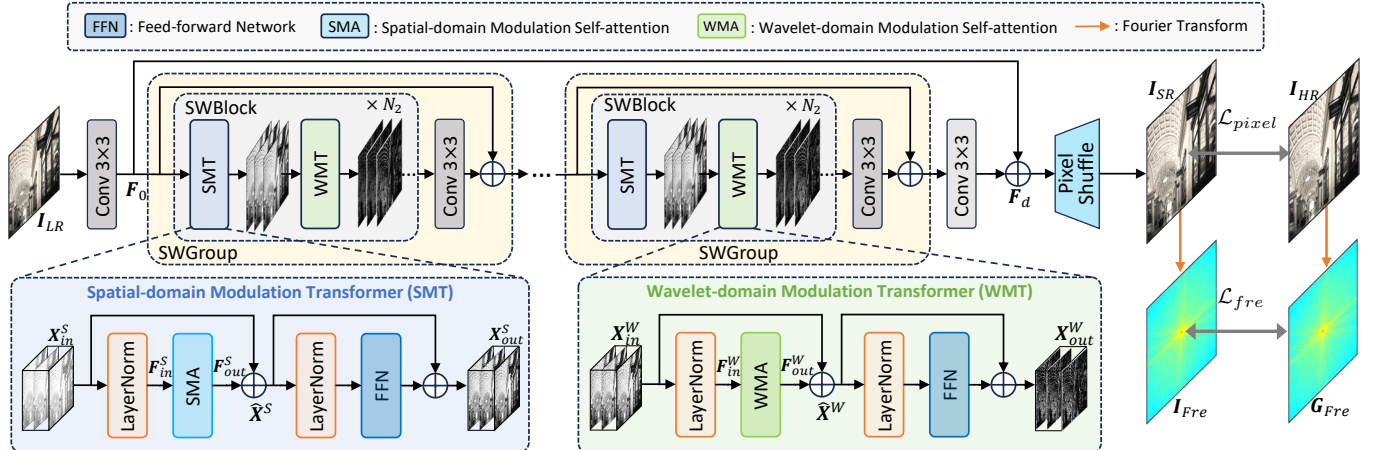


Figure 3: Overview of our method, which utilizes dual modulation in spatial and frequency domains for lightweight SR. Our method comprises N_1 Spatial-Wavelet Groups (SWGroup), each SWGroup comprises N_2 Spatial-Wavelet Blocks (SWBlock).

across self-attention. LBNet [12] and CFIN [36] design efficient architectures to integrate Transformer with CNN. NGswin [15] overcome the disadvantage of the limited receptive field of window-based Transformer. PCTN [37] utilizes multi-scale strategies to enhance the Transformer to explore SR. CAMixSR [7] divides and conquers different area features using CNN and Transformer. However, the above lightweight methods do not utilize frequency domain features. The difference between ours and existing SR methods is shown in TABLE I.

B. Frequency-based SR Methods

Due to their ability to effectively capture different details, frequency-based SR methods have been developed. Specifically, WDRN [38] achieves SR by learning different wavelet coefficients. FADN [39] handles high and low-frequency features separately by networks of different depths. DFSA [40] focuses on utilizing high-frequency information to compensate for textures. JWSGN [22] enhances performance by separately processing features in different wavelet domains. FSR [23] accelerates networks by considering data characteristics in different wavelet domains. DDL [41] improves high-frequency parts by integrating Bayesian methods and frequency inference. FDSR [27] facilitates various features by constructing different frequency networks. Shufflemixer [20], SAFMN [28], and EFHSSR [42] additionally use Fourier supervision to improve SR. FSAS [24] and DF-MSRN [43] integrate Fourier domain information to explore global features for restoration. However, they do not combine the respective strengths of wavelet and Fourier domains to facilitate SR. In contrast, our method combines the advantages of a hybrid frequency domain and presents improved self-attention to make it suitable for exploring various frequency features in the wavelet domain.

III. PROPOSED METHOD

As shown in Fig. 3, an LR image is reconstructed into an accurate SR image in the spatial and frequency domain under the supervision of image reconstruction loss \mathcal{L}_{pixel} and frequency loss \mathcal{L}_{fre} . Our DMNet mainly utilizes our proposed SMT and WMT to modulate the spatial and frequency domain separately.

Specifically, for a LR input $\mathbf{I}_{LR} \in \mathbb{R}^{H \times W \times 3}$, our method aims to obtain a spatial domain SR output $\mathbf{I}_{SR} \in \mathbb{R}^{sH \times sW \times 3}$ and a frequency domain SR output $\mathbf{I}_{Fre} \in \mathbb{R}^{sH \times sW \times 3}$, where s represents the SR scale factor. Specifically, we first extracts its shallow feature $\mathbf{F}_0 \in \mathbb{R}^{H \times W \times C}$. Next, \mathbf{F}_0 is gradually converted to the depth feature $\mathbf{F}_d \in \mathbb{R}^{H \times W \times C}$ through N_1 cascaded SWGroups, where one SWGroup contains N_2 SWBlocks. Finally, Pixel-Shuffle [44] performs convolution, channel and spatial dimension rearrangement operations on \mathbf{F}_d to output an SR image \mathbf{I}_{SR} . Then we acquire the frequency domain SR output \mathbf{I}_{Fre} through Fourier transform.

In the following subsections, we introduce our proposed Wavelet-domain Modulation Transformer and Spatial-domain Modulation Transformer in detail, respectively.

A. Wavelet-domain Modulation Transformer

To facilitate frequency-domain reconstruction, as shown in Fig. 3, we propose a WMT to explore the potential relationship between features in different frequency subbands. As shown in Fig. 4 (c), the core of WMT is to explore the potential relationship between high-frequency and low-frequency features on channels obtained after discrete wavelet transform through our wavelet-domain modulation self-attention. Additionally, a feed-forward network [45] aggregates the obtained frequency domain features. For an input feature $\mathbf{X}_{in}^W \in \mathbb{R}^{H \times W \times C}$ in Fig. 3, the process of obtaining output $\mathbf{X}_{out}^W \in \mathbb{R}^{H \times W \times C}$ can be described as:

$$\hat{\mathbf{X}}^W = \mathcal{WMA} \left(\mathcal{LN} \left(\mathbf{X}_{in}^W \right) \right) + \mathbf{X}_{in}^W, \quad (1)$$

$$\mathbf{X}_{out}^W = \mathcal{FFN} \left(\mathcal{LN} \left(\hat{\mathbf{X}}^W \right) \right) + \hat{\mathbf{X}}^W, \quad (2)$$

where \mathcal{WMA} is our wavelet-domain modulation self-attention. \mathcal{LN} and \mathcal{FFN} have the same meaning as above. Next, we will describe discrete wavelet transform and our wavelet-domain modulation self-attention.

a) *Discrete Wavelet Transform (DWT)*: As shown in Fig. 4 (b), DWT can losslessly convert input $\mathbf{I} \in \mathbb{R}^{H \times W \times C}$ into one low-frequency subband $\mathbf{I}_{LL} \in \mathbb{R}^{\frac{H}{2} \times \frac{W}{2} \times C}$ and three high-frequency subbands $\{\mathbf{I}_{LH}, \mathbf{I}_{HL}, \mathbf{I}_{HH}\} \in \mathbb{R}^{\frac{H}{2} \times \frac{W}{2} \times C}$,

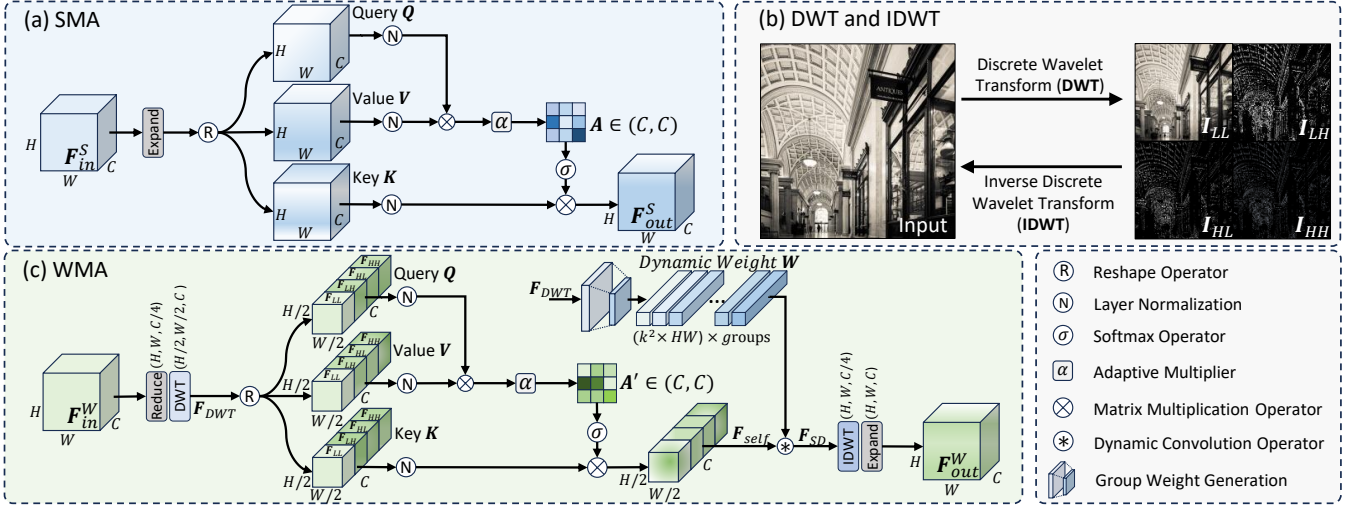


Figure 4: An illustration of (a) our Spatial-domain Modulation Self-attention (SMA), (b) Discrete Wavelet Transform (DWT) and Inverse Discrete Wavelet Transform (IDWT) over an image, (c) our Wavelet-domain Modulation Self-attention (WMA).

where \mathbf{I}_{LL} reflect coarse-grained basic structure of \mathbf{I} , and $\{\mathbf{I}_{LH}, \mathbf{I}_{HL}, \mathbf{I}_{HH}\}$ reflect fine-grained texture details of \mathbf{I} . Specifically, DWT first encodes \mathbf{I} into two subbands $\{\mathbf{I}_L, \mathbf{I}_H\} \in \mathbb{R}^{\frac{H}{2} \times W \times C}$ using a high-pass filter $\mathcal{F}_H = \left(\frac{1}{\sqrt{2}}, \frac{-1}{\sqrt{2}} \right)$ and a low-pass filter $\mathcal{F}_L = \left(\frac{1}{\sqrt{2}}, \frac{1}{\sqrt{2}} \right)$ along rows. Then, \mathcal{F}_L and \mathcal{F}_H are encoded along the columns for \mathbf{I}_L and \mathbf{I}_H to obtain four wavelet subbands $\{\mathbf{I}_{LL}, \mathbf{I}_{LH}, \mathbf{I}_{HL}, \mathbf{I}_{HH}\} \in \mathbb{R}^{\frac{H}{2} \times \frac{W}{2} \times C}$. This process is:

$$\mathbf{I}_L, \mathbf{I}_H = \mathcal{F}_L(\mathbf{I}), \mathcal{F}_H(\mathbf{I}), \quad (3)$$

$$\mathbf{I}_{LL}, \mathbf{I}_{LH}, \mathbf{I}_{HL}, \mathbf{I}_{HH} = \mathcal{F}_L(\mathbf{I}_L, \mathbf{I}_H), \mathcal{F}_H(\mathbf{I}_L, \mathbf{I}_H), \quad (4)$$

as illustrated in the inverse wavelet transform (IDWT) shown in Fig. 4 (b), $\{\mathbf{I}_{LL}, \mathbf{I}_{LH}, \mathbf{I}_{HL}, \mathbf{I}_{HH}\}$ can be losslessly restored to \mathbf{I} . In contrast to the Fourier domain, the wavelet domain emphasizes high-frequency features. Therefore, performing frequency reconstruction of LR images lacking high-frequency features in the wavelet domain is a better solution.

b) Wavelet-domain Modulation Self-attention (WMA):

In our WMA, we employ self-attention and dynamic convolution to modulate different frequency subbands obtained through DWT. Then, we utilize IDWT to restore reconstructed frequency-domain subbands to output features. Therefore, the output will exhibit more accurate frequency domain characteristics. Specifically, as shown in Fig. 4 (c), for an input feature $\mathbf{F}_{in}^W \in \mathbb{R}^{H \times W \times C}$, to reduce Params counts, we first reduce the channels of \mathbf{F}_{in}^W from C to $C/4$ using a convolution layer. Then we utilize DWT to decompose features and concatenate the resulting four wavelet subbands along channels to form frequency feature $\mathbf{F}_{DWT} \in \mathbb{R}^{\frac{H}{2} \times \frac{W}{2} \times C}$:

$$\mathbf{F}_{DWT} = [\mathbf{F}_{LL}, \mathbf{F}_{LH}, \mathbf{F}_{HL}, \mathbf{F}_{HH}] = \mathcal{DWT}(\mathcal{R}(\mathbf{F}_{in}^W)), \quad (5)$$

where \mathcal{R} is channel reduction operator, \mathcal{DWT} is discrete wavelet transform. Next, we extend the frequency domain features of the existing channels and transform to obtain vectors $\{\mathbf{Q}, \mathbf{K}, \mathbf{V}\} \in \mathbb{R}^{C \times \frac{H}{4} \times \frac{W}{4}}$ containing different frequency domain components. As shown in Fig. 4 (c), in channel components

of vectors \mathbf{Q} , \mathbf{K} and \mathbf{V} , the first component is low-frequency component \mathbf{F}_{LL} and other components is high-frequency component $\{\mathbf{F}_{LH}, \mathbf{F}_{HL}, \mathbf{F}_{HH}\}$.

$$\{\mathbf{Q}, \mathbf{K}, \mathbf{V}\} = \mathcal{RS}(\mathcal{D}(\mathcal{P}(\mathbf{F}_{DWT}))), \quad (6)$$

where \mathcal{RS} , \mathcal{D} and \mathcal{P} have the same meaning as earlier. Then, we use self-attention to explore the frequency domain. Specifically, we compute the similarity scores between high- and low-frequency features within the \mathbf{Q} and \mathbf{K} vectors, and use these scores to adaptively extract information from the \mathbf{V} vector, enabling the self-attention mechanism to complement high- and low-frequency information from wavelet-transformed features.

$$\text{Attention}(\mathbf{Q}, \mathbf{K}, \mathbf{V}) = \mathbf{V} \text{Softmax}(\mathbf{Q} \mathbf{K}^T / \alpha), \quad (7)$$

since self-attention does not capture detailed features effectively, we introduce dynamic convolution to adaptively aid our WMA in refining frequency details. Initially, a large kernel group convolution \mathcal{G} is applied to produce a set of dynamic weights \mathbf{W} from wavelet features \mathbf{F}_{DWT} . Then, \mathbf{W} is used to adaptively modulate features \mathbf{F}_{Self} obtained from self-attention, resulting in refined features $\mathbf{F}_{SD} \in \mathbb{R}^{\frac{H}{2} \times \frac{W}{2} \times C}$:

$$\mathbf{F}_{SD} = \text{Attention}(\mathbf{Q}, \mathbf{K}, \mathbf{V}) \circledast \mathcal{G}(\mathbf{F}_{DWT}), \quad (8)$$

where \circledast is the dynamic convolution. Finally, \mathbf{F}_{SD} is reduced to a spatial domain feature after inverse discrete wavelet transform \mathcal{IDWT} . Since its channel count is only $C/4$, we need perform a channel expansion \mathcal{E} to obtain $\mathbf{F}_{out}^W \in \mathbb{R}^{H \times W \times C}$:

$$\mathbf{F}_{out}^W = \mathcal{E}(\mathcal{IDWT}(\mathbf{F}_{SD})), \quad (9)$$

after the modulation process described above, our WMA can accurately recover frequency-domain characteristics, particularly high-frequency features crucial for reconstruction.

B. Spatial-domain Modulation Transformer

To reconstruct features in the spatial domain, as shown in Fig. 3, we propose an SMT. Specifically, we first utilize spatial domain modulation self-attention to estimate spatial

Table II: Quantitative evaluation of our method and existing lightweight SR methods. FLOPs is measured on upsampled images with a spatial size of 1280×720 pixels. The best and second-best results are emphasized in bold and underlined.

Scale	Methods	Params	FLOPs	Set5 [10]	Set14 [11]	BSDS100 [46]	Urban100 [47]	Manga109 [9]
				PSNR/SSIM	PSNR/SSIM	PSNR/SSIM	PSNR/SSIM	PSNR/SSIM
$\times 2$	CARN [33]	1592K	222.8G	37.76/0.9590	33.52/0.9166	32.09/0.8978	31.92/0.9256	38.36/0.9765
	IMDN [13]	694K	158.8G	38.00/0.9605	33.63/0.9177	32.19/0.8996	32.17/0.9283	38.88/0.9774
	SMSR [48]	985K	351.5G	38.00/0.9601	33.64/0.9179	32.17/0.8990	32.19/0.9284	38.76/0.9771
	LatticeNet-CL [49]	756K	169.5G	38.09/0.9608	33.70/0.9188	32.21/0.9000	32.29/0.9291	-
	HPUN-L [14]	714K	151.1G	38.09/0.9608	33.79/0.9198	32.25/0.9006	32.37/0.9307	39.07/0.9779
	DDistill-SR [34]	657K	126.4G	38.08/0.9608	33.73/0.9195	32.25/0.9007	32.39/0.9301	39.16/0.9781
	GASSL-B [19]	689K	158.2G	38.08/0.9607	33.75/0.9194	32.24/0.9005	32.29/0.9298	38.92/0.9777
	SwinIR-light [5]	878K	195.6G	38.14/0.9611	33.86/0.9206	32.31 /0.9012	32.76/0.9340	39.12/0.9783
	LBNet [50]	731K	153.2G	38.05/0.9607	33.65/0.9177	32.16/0.8994	32.30/0.9291	38.88/0.9775
	ELAN-light [6]	582K	168.4G	<u>38.17</u> /0.9611	<u>33.94</u> /0.9207	32.30/0.9012	32.76/0.9340	39.11/0.9782
	NGswin [15]	998K	140.4G	38.05/0.9610	33.79/0.9199	32.27/0.9008	32.53/0.9324	38.97/0.9777
	CFIN [36]	675K	<u>116.9G</u>	38.14/0.9613	33.80/0.9199	32.26/0.9006	32.48/0.9311	38.93/0.9347
	CAMixSR [7]	746K	140.6G	38.16/0.9610	33.90/0.9206	32.31 /0.9010	32.78/0.9329	39.25/0.9779
	FIWHN [16]	705K	137.7G	38.16/0.9613	33.73/0.9194	32.27/0.9007	32.75/0.9337	39.07/0.9782
	DMNet (Ours)	572K	115.7G	38.23/0.9613	33.95/0.9209	32.31/0.9015	32.84/0.9347	39.39/0.9786
$\times 3$	CARN [33]	1592K	118.8G	34.29/0.9255	30.29/0.8407	29.06/0.8034	28.06/0.8493	33.43/0.9427
	IMDN [13]	703K	71.5G	34.36/0.9270	30.32/0.8417	29.09/0.8046	28.17/0.8519	33.61/0.9445
	SMSR [48]	993K	156.8G	34.40/0.9270	30.33/0.8412	29.10/0.8050	28.25/0.8536	33.68/0.9445
	LatticeNet-CL [49]	765K	76.3G	34.46/0.9275	30.37/0.8422	29.12/0.8054	28.23/0.8525	-
	HPUN-L [14]	723K	69.3G	34.56/0.9281	30.45/0.8445	29.18/0.8072	28.37/0.8572	33.90/0.9463
	GASSL-B [19]	691K	70.4G	34.47/0.9278	30.39/0.8430	29.15/0.8063	28.27/0.8546	33.77/0.9455
	DDistill-SR [34]	665K	56.9G	34.43/0.9276	30.39/0.8432	29.16/0.8070	28.31/0.8546	33.97/0.9465
	SwinIR-light [5]	886K	87.2G	<u>34.62</u> /0.9289	<u>30.54</u> /0.8463	29.20/0.8082	28.66/0.8624	33.98/0.9478
	LBNet [12]	691K	70.4G	34.47/0.9277	30.38/0.8417	29.13/0.8061	28.42/0.8559	33.82/0.9460
	ELAN-light [6]	590K	75.7G	34.61/0.9288	30.55 /0.8463	29.21/0.8081	28.69/0.8624	34.00/0.9478
	NGswin [15]	1007K	66.6G	34.52/0.9282	30.53/0.8456	29.19/0.8078	28.52/0.8603	33.89/0.9470
	CFIN [36]	681K	53.5G	34.65/0.9289	30.45/0.8443	29.18/0.8071	28.49/0.8583	33.89/0.9464
	FIWHN [16]	713K	62.0G	34.50/0.9283	30.50/0.8451	29.19/0.8077	28.62/0.8607	33.97/0.9472
	DMNet (Ours)	578K	51.6G	34.71/0.9295	30.56 /0.8459	29.26 /0.8092	28.79 /0.8640	34.35 /0.9488
$\times 4$	CARN [33]	1592K	90.9G	32.13/0.8937	28.60/0.7806	27.58/0.7349	26.07/0.7837	30.42/0.9070
	IMDN [13]	715K	40.9G	32.21/0.8948	28.58/0.7811	27.56/0.7353	26.04/0.7838	30.45/0.9075
	SMSR [48]	1006K	89.1G	32.12/0.8932	28.55/0.7808	27.55/0.7351	26.11/0.7868	30.54/0.9085
	LatticeNet-CL [49]	777K	43.6G	32.30/0.8958	28.65/0.7822	27.59/0.7365	26.19/0.7855	-
	HPUN-L [14]	734K	39.7G	32.31/0.8962	28.73/0.7842	27.66/0.7386	26.27/0.7918	30.77/0.9109
	GASSL-B [19]	694K	39.9G	32.27/0.8962	28.74/0.7850	27.66/0.7388	26.27/0.7914	30.92/0.9122
	DDistill-SR [34]	675K	32.6G	32.29/0.8961	28.69/0.7833	27.65/0.7385	26.25/0.7893	30.79/0.9098
	SwinIR-light [5]	897K	49.6G	32.44/0.8976	28.77/0.7858	27.69/0.7406	26.47/0.7980	30.92/0.9151
	LBNet [12]	742K	38.9G	32.29/0.8960	28.68/0.7832	27.62/0.7382	26.27/0.7906	30.76/0.9111
	ELAN-light [6]	601K	43.2G	32.43/0.8975	<u>28.78</u> /0.7858	27.69/0.7406	26.54/0.7982	30.92/0.9150
	NGswin [15]	1019K	36.4G	32.33/0.8963	<u>28.78</u> /0.7859	27.66/0.7396	26.45/0.7963	30.80/0.9128
	CFIN [36]	699K	<u>31.2G</u>	32.49/0.8985	28.74/0.7849	27.68/0.7396	26.39/0.7946	30.73/0.9124
	CAMixSR [7]	765K	37.8G	<u>32.45</u> /0.8978	<u>28.78</u> /0.7856	27.69/0.7401	26.51/0.7966	31.06/0.9148
	FIWHN [16]	725K	35.6G	32.30/0.8967	28.76/0.7849	27.68/0.7400	26.57/0.7989	30.93/0.9131
	DMNet (Ours)	587K	29.8G	32.51 /0.8987	28.84 /0.7866	27.73 /0.7410	26.58 /0.7991	31.14 /0.9150

domain features. Subsequently, a feed-forward network [45] based on CNN is utilized to aggregate features to refine representation. For an input $\mathbf{X}_{in}^S \in \mathbb{R}^{H \times W \times C}$ in Fig. 3, the process of obtaining output $\mathbf{X}_{out}^S \in \mathbb{R}^{H \times W \times C}$ is:

$$\hat{\mathbf{X}}^S = \text{SMA} \left(\mathcal{LN} \left(\mathbf{X}_{in}^S \right) \right) + \mathbf{X}_{in}^S, \quad (10)$$

$$\mathbf{X}_{out}^S = \mathcal{FFN} \left(\mathcal{LN} \left(\hat{\mathbf{X}}^S \right) \right) + \hat{\mathbf{X}}^S, \quad (11)$$

where \mathcal{LN} is layer normalization, SMA is our spatial-domain modulation self-attention, and \mathcal{FFN} is feed-forward network, respectively. The core part is spatial-domain modulation self-attention, we will detail this component below.

a) Spatial-domain Modulation Self-attention (SMA):

In our SMA, to estimate spatial-domain features with less consumption, our SMA condenses extracted spatial domain features in channels and implicitly estimates global spatial domain features by performing self-attention over channels.

As shown in Fig. 4 (a), for an input $\mathbf{F}_{in}^S \in \mathbb{R}^{H \times W \times C}$, we first utilize a 1×1 point-wise convolution \mathcal{P} and a 3×3 depth-wise convolution \mathcal{D} to expand channels and extract features. Then, query $\mathbf{Q} \in \mathbb{R}^{C \times HW}$, key $\mathbf{K} \in \mathbb{R}^{C \times HW}$, and value $\mathbf{V} \in \mathbb{R}^{C \times HW}$ are obtained by performing a reshape operation \mathcal{RS} on channel space. This process is:

$$\{\mathbf{Q}, \mathbf{K}, \mathbf{V}\} = \mathcal{RS} \left(\mathcal{D} \left(\mathcal{P} \left(\mathbf{F}_{in}^S \right) \right) \right), \quad (12)$$

next, normalization-operated vectors \mathbf{Q} , \mathbf{K} , \mathbf{V} explore potential

Table III: Quantitative evaluation with more Transformer/Mamba-based lightweight SR methods. FLOPs and speed are measured on upsampled images with a spatial size of 1280×720 pixels. Memory is measured when batch size is 16 and patch size is 64.

Scale	Methods	Params	FLOPs	Speed	Memory	Set5 [10]	Set14 [11]	BSDS100 [46]	Urban100 [47]	Manga109 [9]	Average
						PSNR/SSIM	PSNR/SSIM	PSNR/SSIM	PSNR/SSIM	PSNR/SSIM	PSNR/SSIM
$\times 2$	SwinIR-light [5]	878K	195.6G	1.30s	8.0G	38.14/0.9611	33.86/0.9206	32.31/0.9012	32.76/0.9340	39.12/0.9783	35.24/0.9390
	DLGSANet-light [1]	745K	170.0G	0.11s	9.9G	38.20/0.9612	33.89/0.9203	32.30/0.9012	32.94/0.9355	39.29/0.9780	35.32/0.9392
	SRFormer-light [1]	853K	236.2G	1.39s	8.7G	38.23/0.9613	33.94/0.9209	32.36/0.9019	32.91/0.9353	39.28/0.9779	35.36/0.9394
	HiT-SNG [18]	1013K	213.9G	0.24s	16.6G	38.21/0.9612	34.00/0.9217	32.35/0.9019	33.01/0.9360	39.32/0.9782	35.38/0.9396
	MambaIR [2]	879K	198.1G	0.49s	16.7G	38.16/0.9610	34.00/0.9212	32.34/0.9017	32.92/0.9356	39.31/0.9779	35.35/0.9394
	DMNet (Ours)	572K	115.7G	0.07s	7.0G	38.23/0.9613	33.95/0.9209	32.31/0.9015	32.84/0.9347	39.39/0.9786	35.35/0.9394
	DMNet-L (Ours)	733K	147.4G	0.09s	9.1G	38.27/0.9615	34.00/0.9212	32.34/0.9017	32.98/0.9359	39.52/0.9791	35.42/0.9399

relationships of spatial domain features within channels through self-attention, which in turn reconstruct spatial domain pixel distribution. This process can be formulated as:

$$\text{Attention}(\mathbf{Q}, \mathbf{K}, \mathbf{V}) = \mathbf{V} \text{Softmax}(\mathbf{Q}\mathbf{K}^T/\alpha), \quad (13)$$

where α is a learnable factor, after several SMA and WMA blocks, we get a depth feature \mathbf{F}_d . Finally, we get an SR image \mathbf{I}_{SR} from \mathbf{F}_d after a Pixel-Shuffle [44].

C. Loss Function

For image pairs $\{\mathbf{I}_{SR}, \mathbf{I}_{HR}\}$ in training, a reconstruction loss \mathcal{L}_{pixel} is used for supervising spatial-domain SR:

$$\mathcal{L}_{pixel} = \|\mathbf{I}_{SR} - \mathbf{I}_{HR}\|_1, \quad (14)$$

where \mathbf{I}_{SR} is the SR result of our method, \mathbf{I}_{HR} is ground truth. Further, we introduce the frequency loss \mathcal{L}_{fre} in our frequency domain output \mathbf{I}_{Fre} of amplitude \mathbf{A}_{SR} and phase \mathbf{P}_{SR} to ensure the accuracy of the frequency domain SR:

$$\mathcal{L}_{fre} = \|[\mathbf{A}_{SR}, \mathbf{P}_{SR}] - [\mathbf{A}_{HR}, \mathbf{P}_{HR}]\|_1, \quad (15)$$

where \mathbf{A}_{HR} and \mathbf{P}_{HR} are the amplitude and phase of frequency domain ground truth \mathbf{G}_{Fre} . The Fourier loss promotes model convergence more effectively than the potential conflicts between different wavelet subbands during gradient updates, which require careful parameter tuning. Therefore, We use Fourier loss. Finally, our total loss is:

$$\mathcal{L}_{total} = \mathcal{L}_{pixel} + \lambda \mathcal{L}_{fre}, \quad (16)$$

where λ is a hyper-parameter that is set to 10^{-1} .

IV. EXPERIMENTS

We compare our method with existing lightweight SR methods on synthetic and real datasets, followed by ablations to analyze the effectiveness of our proposed module.

A. Experimental Settings

1) *Datasets.*: Our method is trained on the DIV2K [51] dataset which contains 800 pairs of training images. To evaluate our method, we test on commonly used synthetic test datasets, including Set5 [10], Set14 [11], BSDS100 [46], Urban100 [47], and Manga109 [9]. We also train and evaluate our method on the real-world dataset RealSRV3 [52], which obtains LR-HR image pairs on the same scene by adjusting the focal length of a digital camera and alignment operations to images to simulink blurred LR images.

Table IV: Quantitative evaluation of our method and existing lightweight SR methods on a real-world test set.

Scale	Methods	Params	FLOPs	RealSRV3 [52]	
				PSNR↑/SSIM↑/LPIPS↓	
$\times 4$	IMDN [13]	715K	40.9G	29.20/0.8264/0.2810	
	SwinIR-light [5]	897K	49.6G	29.18/0.8278/0.2756	
	ELAN-light [6]	601K	43.2G	29.20/0.8272/0.2764	
	NGswin [15]	1019K	36.4G	29.06/0.8240/0.2779	
	MambaIR [2]	879K	50.6G	29.22/0.8286/0.2748	
	DMNet (Ours)	587K	29.8G	29.27/0.8295/0.2739	

2) *Metrics and Implementation Details.*: We calculate PSNR and SSIM [53] values as evaluation metrics on the Y channel in the YCbCr color space. We additionally employ LPIPS [54] for evaluating the real-world test set. During training, we set the batch size to 64, the initial learning rate to 5×10^{-4} with a scheduler in 500K iterations, and the patch size is set to 64×64 . We train our method using Adam optimizer with $\beta_1=0.9$, $\beta_2=0.99$. We implement all experiments using the Pytorch framework with the NVIDIA GeForce RTX 4090. In our DMNet, we set N_1 to 3, N_2 to 3, and the number of feature channels to 48.

B. Comparisons with State-of-the-Art Methods

To evaluate the effectiveness of our method, we compare our method with several state-of-the-art methods, including CNN-based methods CARN [33], IMDN [13], GASSL-B [19] and Transformer-based methods SwinIR-light [5], ELAN-light [6], NGswin [15], CAMixSR [7].

1) *Comparison on Synthesized Datasets*: TABLE II presents the results of quantitative comparisons among various lightweight SR methods at scale factors of $\times 2$, $\times 3$, and $\times 4$. With minimal model computational costs, our DMNet outperforms state-of-the-art methods in terms of PSNR and SSIM on all benchmark test datasets. Specifically, compared to the latest CNN-based method GASSL-B [19], we surpass its PSNR by 0.24dB, 0.26dB, and 0.19dB at three scale factors, respectively, while utilizing only 83% of its number of parameters and 72% of its FLOPs. Compared to the latest Transformer-based method NGswin [15], we surpass its PSNR by 0.18dB, 0.14dB, and 0.16dB at three scale factors, respectively, while utilizing only 57% of its number of parameters and 82% of its FLOPs. In Fig. 5, we present a visual comparison of existing methods at three scale factors. We observe that our method accurately reconstructs high-frequency boundaries of walls, railings, and letters, highlighting the texture

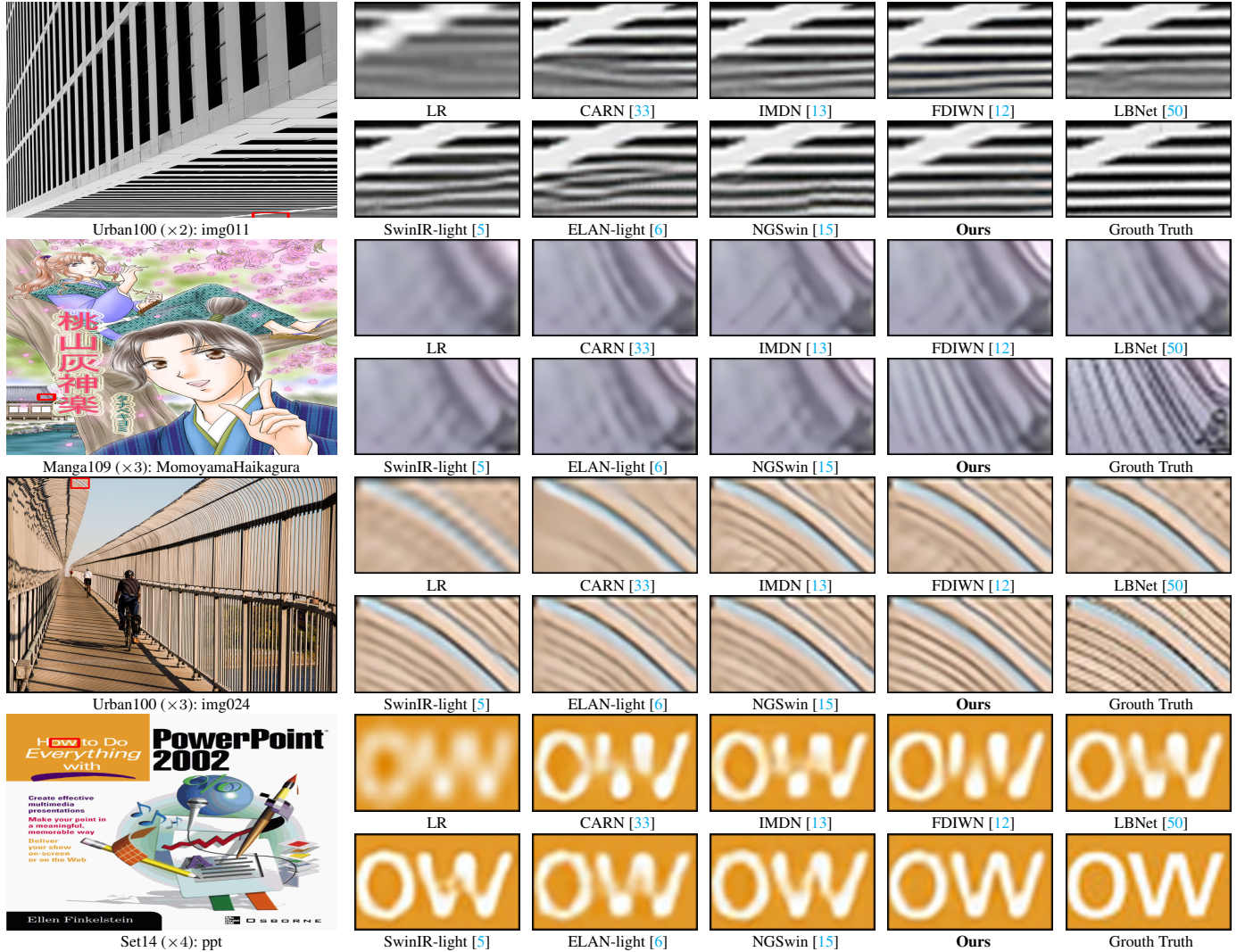


Figure 5: Qualitative comparisons with existing methods on the synthesized test set. Our method can reconstruct clearer edges.

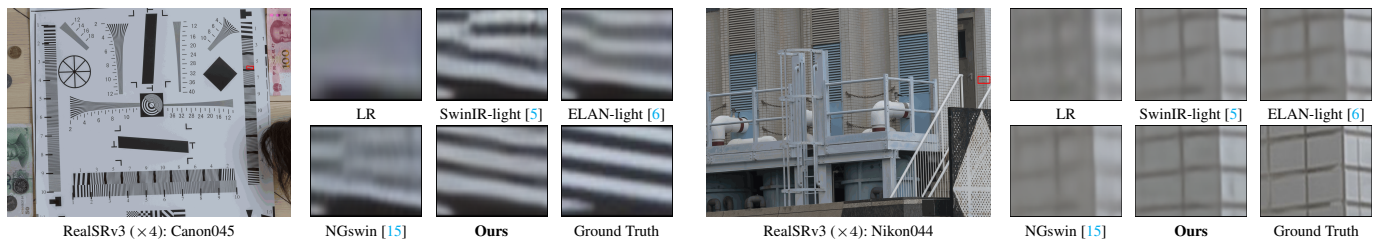


Figure 6: Qualitative comparisons with existing methods on the real-world test set RealSRv3 [52].

of image contours. In contrast, images reconstructed by existing methods appear blurry or incorrect textures. The quantitative and qualitative results all show the superiority of our method in terms of lightweight and performance.

Moreover, we contrast our method with existing methods using the interpretability analysis tool LAM [8] to examine the pixel range utilized for SR reconstruction. LAM can illustrate the correlation between each pixel and the patch outlined in red during the inference process. The diffusion index (DI) and pixel contribution regions are depicted in Fig 7, where a higher DI or more pixel contribution regions signify a broader

range of pixels engaged in the model. Our method's higher DI value and broader pixel contribution area compared to existing methods indicate that it captures more contextual information, showcasing the effectiveness of utilizing wavelet domain information and Fourier domain supervision simultaneously. In addition, Figure 8 shows corresponding visual comparisons. Our method not only has higher LAM scores but also has clearer and more accurate SR reconstruction results in corresponding image red patches than existing methods.

2) *Comparison on Real-world Datasets:* We conduct experiments on RealSRv3 [52], which generates LR and HR

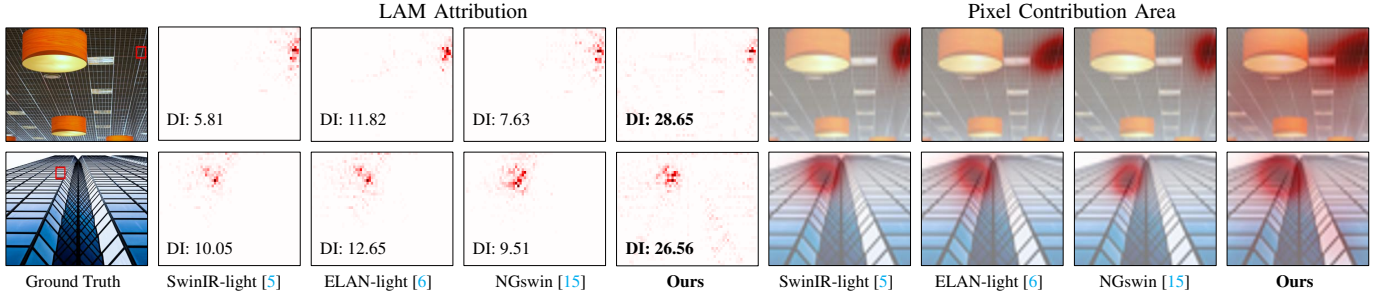


Figure 7: Comparison with existing methods on LAM [8] results. LAM [8] indicates the pixel range utilized by the network when inferring the SR image for the portion outlined with the red box. DI quantifies the results of LAM [8], with our method achieving the highest DI score and the widest pixel contribution area, indicating its ability to capture broader features.

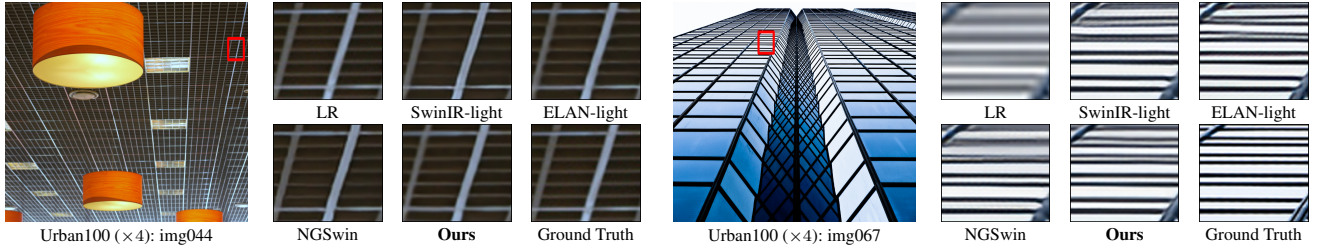


Figure 8: Qualitative comparisons with existing Transformer-based methods.

image pairs of real scenes by modulating camera focal lengths. TABLE IV presents the results of quantitative comparisons with IMDN [13], SwinIR-light [5], ELAN-light [6], NGswin [15], and MambaIR [2] at scale factors of $\times 4$. Our method reconstructs images with higher pixel similarity metrics, such as PSNR and SSIM, as well as perceptual metrics, like LPIPS, at lower computational costs compared to existing lightweight methods. Additionally, including Nikon and Canon datasets, Fig. 6 compares visual results in real-world datasets, where our method reconstructs sharper image textures and closely resembles the ground truth compared to existing methods.

3) *Model Efficiency Tradeoffs*: TABLE III shows a comprehensive comparison with existing lightweight Transformer- and Mamba-based SR methods, including the number of Parmas, number of FLOPs, inference time, GPU memory, and performance at the scale of $\times 2$. Our method boasts the smallest model size and GPU memory, the fastest inference, and optimal PSNR across various scenarios. Notably, our WMT enables interactions between different frequency subbands within a sensory field downsampled by a factor of 2, significantly accelerating inference by $1.6\times$ to $15.4\times$ compared to existing Transformer- and Mamba-based methods. The comparisons unequivocally showcase the superiority of our method in terms of both lightweight, performance, and inference speed.

C. Ablation Studies

In ablation studies, we mainly discuss the design of WMA and DMNet configurations and the effectiveness of WMA, including comparing with existing self-attentions and CNNs.

1) *Ablation Study on WMA Configurations*: In TABLE V, we conduct an ablation study to investigate the effect of various components in WMA, including the following variants:

Case1: The selection of frequency domain includes the wavelet domain after the wavelet transform and the Fourier domain after the Fourier transform. **Case2:** The selection of frequency loss for supervising the frequency domain reconstruction includes Wavelet loss and Fourier loss as described in subsection III-C. **Case3:** The selection of the internal module structure of WMA includes a dynamic branch responsible for enhancing frequency domain details. By combining Case1 and Case2, it is evident that selecting the wavelet transform as the frequency decomposition function, with Fourier loss supervision, is the optimal choice for achieving accurate SR results at lower computational costs. As shown in Fig 11, wavelet information and Fourier information facilitate the recovery of high-frequency features and overall structure, respectively. Moreover, the dynamic weight within WMA significantly aids in reconstruction, resulting in a PSNR improvement of 0.06dB with an increase in the number of parameters of less than 4k. Therefore, the above cases fully justify our design of WMA.

2) *Ablation Study on DMNet Configurations*: To validate the robustness of our DMNet configuration, we present a series of ablations in Fig 9, which includes the following variants:

Case1: The benefits of focusing on both spatial and frequency domain information. As depicted in Fig 9 (a), when supervised by both spatial and frequency losses, concentrating on both spatial and frequency domain feature reconstruction leads to faster convergence and superior performance compared to focusing solely on the spatial or frequency domain without incurring too much computational consumption.

Case2: The optimal ratio of modules that concentrate on the spatial domain to those that focus on the frequency domain. In

Table V: Ablation on configurations of wavelet-domain modulation self-attention (WMA) at scale factors of $\times 4$. “Wavelet domain” and “Fourier domain” refer to the choice of frequency domain chose within WMA. “Wavelet loss” and “Fourier loss” refer to the choice of frequency loss. “Dynamic” refers to the dynamic weight in WMA.

Methods	Frequency Domain		Frequency Loss		Module Structure	Params	FLOPs	Set5	
	Wavelet domain	Fourier domain	Wavelet loss	Fourier loss				PSNR	SSIM
w/o Dynamic	✓				✗	79.8K	4.15G	31.57	0.8853
Model1		✓	✓		✓	84.8K	4.82G	31.57	0.8846
Model2		✓		✓	✓	84.8K	4.82G	31.56	0.8842
Model3	✓		✓		✓	83.6K	4.19G	31.54	0.8837
Ours	✓			✓	✓	83.6K	4.19G	31.63	0.8858

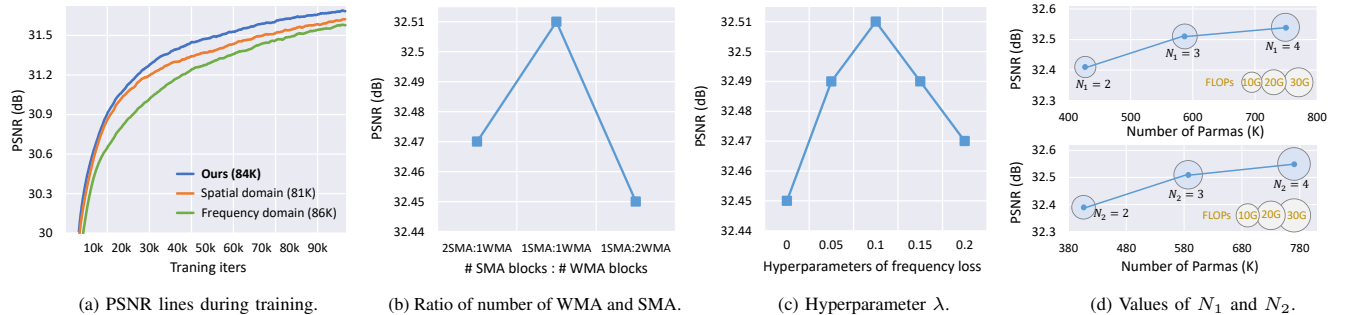


Figure 9: Ablation studies of our DMNet at scale factors of $\times 4$ on Set5 [10] test set, where all methods in (a) use the loss of Eq.(16). N_1 and N_2 refer to the number of SWBlock and SWGroup in Fig 3.

our DMNet, employing SMA for the spatial domain and WMA for the frequency domain, we aim to determine the optimal ratio between the two modules. Fig 9 (b) demonstrates that the one-to-one ratio currently employed in our method is optimal.

Case3: Ablation study on the hyperparameter λ of the frequency loss. Fig 9 (c) shows that incorporating frequency loss supervision enhances the model’s performance, with the optimal performance achieved at $\lambda = 0.1$. Deviating too much or too little from this value can negatively impact performance, thus justifying our choice of $\lambda = 0.1$ for our DMNet.

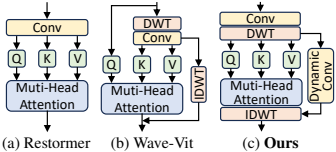


Figure 10: Comparison of our proposed WMA and self-attention in Restormer [45] and Wave-Vit [55].

Case4: Impact of values of N_1 and N_2 on performance. In our DMNet in Fig 3, we partition the combined SMT and WMT structure into distinct SWBlocks and SWGroups, which are then interconnected using residual connections. Fig 9 (d) investigates the optimal selection of the number of N_1 and N_2 . As N_1 and N_2 increase from 2 to 3, there is a rise in PSNR of nearly 0.1 dB, accompanied by a certain increase in computational consumption. However, when N_1 and N_2 are increased from 3 to 4, the gain in PSNR is relatively smaller, even though the computational consumption increases further. Consequently, in our DMNet, we choose $N_1 = N_2 = 3$.

Table VI: Quantitative evaluation of our WMA and related self-attention modules.

Modules	(a)	(b)	Ours
Parmas \downarrow	80.9K	102.7K	83.6K
FLOPs \downarrow	4.7G	7.1G	4.2G
Memory \downarrow	2.12G	9.66G	1.96G
PSNR \uparrow	31.56	31.39	31.63
SSIM \uparrow	0.8844	0.8811	0.8858

3) Comparison of WMA and Existing Self-attentions: As shown in Fig 10, We give structural differences between ours and relevant self-attentions. Compared to Restormer [45] and Wave-Vit [55], which have a computational complexity of $\mathcal{O}(C^2N)$ and $\mathcal{O}(N^2C/16)$, respectively, our computational complexity is smaller, only $\mathcal{O}(C^2N/4)$, where $N = H \times W$, H , W , C are the height, width, and number of channels of the feature, respectively. Additionally, TABLE VI shows our WMA can achieve SR more efficiently than these methods, including computational costs, GPU memory in training, and performance on the Set5 test set. Hence, our WMA is a better solution for frequency-based SR than existing self-attentions.

4) Effectiveness of WMT: In this part, we first show the effect of our WMT compared to existing frequency-based SR modules. These comparison modules include methods from CNN-based and transformer-based methods for processing wavelet and Fourier features. Notably, these frequency-domain processing modules originate from general SR methods, as lightweight SR currently lacks dedicated modules for frequency-domain exploration. As shown in TABLE VII, compared to these modules, our WMT is more efficient, achieving higher

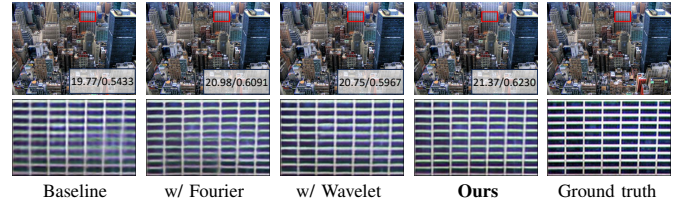


Figure 11: Fourier and Wavelet domain information facilitates the reconstruction of accurate overall structure (PSNR and SSIM) and sharp SR textures.

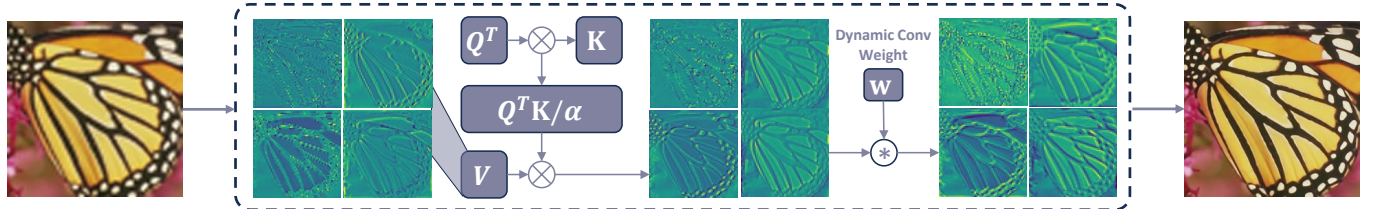


Figure 12: Visualization of features within our WMA. First, self-attention learns relationships between high and low-frequency information in the wavelet domain, enabling mutual enhancement to reconstruct global dependencies. Then, dynamic convolution adaptively captures the details of each frequency component to refine local features.

Table VII: Ablation study on existing frequency-based modules, including WTM in JWSGN [22], FSAS in FFTformer [24], WaveMix in WaveMixSR [56], and WAT in SODA-SR [30], with our proposed WMT, on the $\times 4$ Set5 [9] test set.

Modules	Params	FLOPs	Speed	PSNR / SSIM
WTM [22]	134.3K	5.49G	90ms	31.43 / 0.8840
FSAS [24]	137.2K	7.90G	35ms	31.51 / 0.8845
WaveMix [56]	146.2K	5.76G	46ms	31.41 / 0.8839
WAT [30]	126.3K	5.51G	129ms	31.55 / 0.8849
Ours	83.6K	4.19G	26ms	31.63 / 0.8858

PSNR/SSIM with lower computational cost and faster inference. This demonstrates that our WMT is better suited for lightweight frequency domain exploration.

Next, we present a feature map visualization of the self-attention part (WMA) within the WMT interior to highlight the role of wavelet transform combined with self-attention and dynamic convolution. As shown in Fig 12, for input features with one low-frequency component and three high-frequency components, self-attention improves global textures by capturing long-range dependencies, leading to a more coherent overall structure. However, it fails to fully capture subtle low-frequency details. Dynamic convolution complements this by adaptively refining these details, ensuring that both global structures and fine-grained local features are accurately restored, thus enhancing the overall quality of feature maps.

V. LIMITATIONS AND FUTURE WORKS

While our proposed DMNet achieves competitive results in lightweight SR, there are several areas for improvement. The model could be further optimized for extremely LR images, where the current SR performance may not be as robust. Additionally, more advanced fusion techniques between frequency and spatial domains could enhance the overall feature extraction and reconstruction process. The scalability of the model for larger datasets and real-time applications also remains a challenge. Future work could focus on enhancing the model's efficiency and robustness for diverse SR scenarios, improving its deployment on resource-constrained devices, and exploring its applicability to more low-level vision tasks.

VI. CONCLUSION

This paper presents a dual-domain modulation network for lightweight SR. We introduce SMT and WMT to address

reconstruction in the spatial and frequency domains to enhance performance while maintaining lightweight. Meanwhile, the above process is supervised through image reconstruction and Fourier loss. We show that by combining wavelet features with Fourier supervision, our WMT can reconstruct high-frequency features while maintaining overall quality. Further, WMT as a frequency domain exploration module designed for lightweight SR, effectively enhances SR with minimal overhead. Through extensive experiments on both synthesized and real datasets, we show our method achieves superior performance with lower complexity, surpassing state-of-the-art lightweight SR methods.

REFERENCES

- [1] Y. Zhou, Z. Li, C.-L. Guo, S. Bai, M.-M. Cheng, and Q. Hou, “Srformer: Permuted self-attention for single image super-resolution,” in *ICCV*, 2023, pp. 12 780–12 791. [1](#), [6](#)
- [2] H. Guo, J. Li, T. Dai, Z. Ouyang, X. Ren, and S.-T. Xia, “Mambair: A simple baseline for image restoration with state-space model,” in *ECCV*. Springer, 2025, pp. 222–241. [1](#), [6](#), [8](#)
- [3] B. Lim, S. Son, H. Kim, S. Nah, and K. Mu Lee, “Enhanced deep residual networks for single image super-resolution,” in *CVPRW*, 2017, pp. 136–144. [1](#)
- [4] T. Dai, J. Cai, Y. Zhang, S.-T. Xia, and L. Zhang, “Second-order attention network for single image super-resolution,” in *CVPR*, 2019, pp. 11 065–11 074. [1](#)
- [5] J. Liang, J. Cao, G. Sun, K. Zhang, L. Van Gool, and R. Timofte, “Swinir: Image restoration using swin transformer,” in *ICCVW*, 2021, pp. 1833–1844. [1](#), [2](#), [5](#), [6](#), [7](#), [8](#)
- [6] X. Zhang, H. Zeng, S. Guo, and L. Zhang, “Efficient long-range attention network for image super-resolution,” in *ECCV*. Springer, 2022, pp. 649–667. [1](#), [2](#), [5](#), [6](#), [7](#), [8](#)
- [7] Y. Wang, Y. Liu, S. Zhao, J. Li, and L. Zhang, “Camixersr: Only details need more” attention”, in *Proceedings of the IEEE/CVF Conference on Computer Vision and Pattern Recognition*, 2024, pp. 25 837–25 846. [1](#), [3](#), [5](#), [6](#)
- [8] J. Gu and C. Dong, “Interpreting super-resolution networks with local attribution maps,” in *CVPR*, 2021, pp. 9199–9208. [1](#), [7](#), [8](#)
- [9] Y. Matsui, K. Ito, Y. Aramaki, A. Fujimoto, T. Ogawa, T. Yamasaki, and K. Aizawa, “Sketch-based manga retrieval using manga109 dataset,” *Multimedia Tools and Applications*, vol. 76, pp. 21 811–21 838, 2017. [1](#), [5](#), [6](#), [10](#)
- [10] M. Bevilacqua, A. Roumy, C. Guillemot, and M. L. Alberi-Morel, “Low-complexity single-image super-resolution based on nonnegative neighbor embedding,” vol. 135, pp. 1–10, 2012. [1](#), [5](#), [6](#), [9](#)
- [11] R. Zeyde, M. Elad, and M. Protter, “On single image scale-up using sparse-representations,” in *ICCS*. Springer, 2012, pp. 711–730. [1](#), [5](#), [6](#)
- [12] G. Gao, W. Li, J. Li, F. Wu, H. Lu, and Y. Yu, “Feature distillation interaction weighting network for lightweight image super-resolution,” in *AAAI*, vol. 36, no. 1, 2022, pp. 661–669. [1](#), [2](#), [3](#), [5](#), [7](#)
- [13] Z. Hui, X. Gao, Y. Yang, and X. Wang, “Lightweight image super-resolution with information multi-distillation network,” in *ACMMM*, 2019, pp. 2024–2032. [1](#), [2](#), [5](#), [6](#), [7](#), [8](#)
- [14] B. Sun, Y. Zhang, S. Jiang, and Y. Fu, “Hybrid pixel-unshuffled network for lightweight image super-resolution,” in *AAAI*, vol. 37, no. 2, 2023, pp. 2375–2383. [1](#), [5](#)

[15] H. Choi, J. Lee, and J. Yang, "N-gram in swin transformers for efficient lightweight image super-resolution," in *CVPR*, 2023, pp. 2071–2081. [1](#), [3](#), [5](#), [6](#), [7](#), [8](#)

[16] W. Li, J. Li, G. Gao, W. Deng, J. Yang, G.-J. Qi, and C.-W. Lin, "Efficient image super-resolution with feature interaction weighted hybrid network," *IEEE Transactions on Multimedia*, 2024. [1](#), [2](#), [5](#)

[17] X. Li, J. Dong, J. Tang, and J. Pan, "Dlgsanet: lightweight dynamic local and global self-attention networks for image super-resolution," in *ICCV*, 2023, pp. 12792–12801. [1](#)

[18] X. Zhang, Y. Zhang, and F. Yu, "Hit-sr: Hierarchical transformer for efficient image super-resolution," in *ECCV*. Springer, 2025, pp. 483–500. [1](#), [6](#)

[19] H. Wang, Y. Zhang, C. Qin, L. Van Gool, and Y. Fu, "Global aligned structured sparsity learning for efficient image super-resolution," *IEEE Transactions on Pattern Analysis and Machine Intelligence*, vol. 45, no. 9, pp. 10974–10989, 2023. [1](#), [5](#), [6](#)

[20] L. Sun, J. Pan, and J. Tang, "Shufflemixer: An efficient convnet for image super-resolution," in *NeurIPS*, vol. 35, 2022, pp. 17314–17326. [1](#), [2](#), [3](#)

[21] L. Sun, J. Dong, J. Tang, and J. Pan, "Spatially-adaptive feature modulation for efficient image super-resolution," in *ICCV*, 2023, pp. 13190–13199. [1](#)

[22] W. Zou, L. Chen, Y. Wu, Y. Zhang, Y. Xu, and J. Shao, "Joint wavelet sub-bands guided network for single image super-resolution," *IEEE Transactions on Multimedia*, 2022. [1](#), [2](#), [3](#), [10](#)

[23] J. Li, T. Dai, M. Zhu, B. Chen, Z. Wang, and S.-T. Xia, "Fsr: A general frequency-oriented framework to accelerate image super-resolution networks," in *AAAI*, vol. 37, no. 1, 2023, pp. 1343–1350. [1](#), [2](#), [3](#)

[24] L. Kong, J. Dong, J. Ge, M. Li, and J. Pan, "Efficient frequency domain-based transformers for high-quality image deblurring," in *CVPR*, 2023, pp. 5886–5895. [1](#), [2](#), [3](#), [10](#)

[25] X. Jiang, N. Wang, J. Xin, K. Li, X. Yang, J. Li, X. Wang, and X. Gao, "Fabnet: Frequency-aware binarized network for single image super-resolution," *IEEE Transactions on Image Processing*, vol. 32, pp. 6234–6247, 2023. [1](#)

[26] M. Zheng, L. Sun, J. Dong, and J. Pan, "Smfanet: A lightweight self-modulation feature aggregation network for efficient image super-resolution," in *ECCV*. Springer, 2025, pp. 359–375. [2](#)

[27] P. Xu, Q. Liu, H. Bao, R. Zhang, L. Gu, and G. Wang, "Fdsr: An interpretable frequency division stepwise process based single-image super-resolution network," *IEEE Transactions on Image Processing*, 2024. [2](#), [3](#)

[28] S. Guo, H. Yong, X. Zhang, J. Ma, and L. Zhang, "Spatial-frequency attention for image denoising," *arXiv preprint arXiv:2302.13598*, 2023. [2](#), [3](#)

[29] W. Li, H. Guo, X. Liu, K. Liang, J. Hu, Z. Ma, and J. Guo, "Efficient face super-resolution via wavelet-based feature enhancement network," in *Proceedings of the 32nd ACM International Conference on Multimedia*, 2024, pp. 4515–4523. [2](#)

[30] Y. Ai, X. Zhou, H. Huang, L. Zhang, and R. He, "Uncertainty-aware source-free adaptive image super-resolution with wavelet augmentation transformer," in *CVPR*, 2024, pp. 8142–8152. [2](#), [10](#)

[31] J. Li, Z. Pei, W. Li, G. Gao, L. Wang, Y. Wang, and T. Zeng, "A systematic survey of deep learning-based single-image super-resolution," *ACM Computing Surveys*, vol. 56, no. 10, pp. 1–40, 2024. [2](#)

[32] C. Dong, C. C. Loy, and X. Tang, "Accelerating the super-resolution convolutional neural network," in *ECCV*. Springer, 2016, pp. 391–407. [2](#)

[33] N. Ahn, B. Kang, and K.-A. Sohn, "Fast, accurate, and lightweight super-resolution with cascading residual network," in *ECCV*, 2018, pp. 252–268. [2](#), [5](#), [6](#), [7](#)

[34] Y. Wang, T. Su, Y. Li, J. Cao, G. Wang, and X. Liu, "Ddistill-sr: Reparameterized dynamic distillation network for lightweight image super-resolution," *IEEE Transactions on Multimedia*, vol. 25, pp. 7222–7234, 2023. [2](#), [5](#)

[35] K. Park, J. W. Soh, and N. I. Cho, "A dynamic residual self-attention network for lightweight single image super-resolution," *IEEE Transactions on Multimedia*, vol. 25, pp. 907–918, 2021. [2](#)

[36] W. Li, J. Li, G. Gao, W. Deng, J. Zhou, J. Yang, and G.-J. Qi, "Cross-receptive focused inference network for lightweight image super-resolution," *IEEE Transactions on Multimedia*, vol. 26, pp. 864–877, 2024. [3](#), [5](#)

[37] M. Li, B. Ma, and Y. Zhang, "Lightweight image super-resolution with pyramid clustering transformer," *IEEE Transactions on Circuits and Systems for Video Technology*, 2023. [3](#)

[38] J. Xin, J. Li, X. Jiang, N. Wang, H. Huang, and X. Gao, "Wavelet-based dual recursive network for image super-resolution," *IEEE Transactions on Neural Networks and Learning Systems*, vol. 33, no. 2, pp. 707–720, 2020. [3](#)

[39] W. Xie, D. Song, C. Xu, C. Xu, H. Zhang, and Y. Wang, "Learning frequency-aware dynamic network for efficient super-resolution," in *ICCV*, 2021, pp. 4308–4317. [3](#)

[40] S. A. Magid, Y. Zhang, D. Wei, W.-D. Jang, Z. Lin, Y. Fu, and H. Pfister, "Dynamic high-pass filtering and multi-spectral attention for image super-resolution," in *ICCV*, 2021, pp. 4288–4297. [3](#)

[41] T. Liu, J. Cheng, and S. Tan, "Spectral bayesian uncertainty for image super-resolution," in *CVPR*, 2023, pp. 18166–18175. [3](#)

[42] J. Song, A. Sowmya, and C. Sun, "Efficient hybrid feature interaction network for stereo image super-resolution," *IEEE Transactions on Multimedia*, 2024. [3](#)

[43] Y. Ju, J. Xiao, C. Zhang, H. Xie, A. Luo, H. Zhou, J. Dong, and A. C. Kot, "Towards marine snow removal with fusing fourier information," *Information Fusion*, vol. 117, p. 102810, 2025. [3](#)

[44] W. Shi, J. Caballero, F. Huszár, J. Totz, A. P. Aitken, R. Bishop, D. Rueckert, and Z. Wang, "Real-time single image and video super-resolution using an efficient sub-pixel convolutional neural network," in *CVPR*, 2016, pp. 1874–1883. [3](#), [6](#)

[45] S. W. Zamir, A. Arora, S. Khan, M. Hayat, F. S. Khan, and M.-H. Yang, "Restormer: Efficient transformer for high-resolution image restoration," in *CVPR*, 2022, pp. 5728–5739. [3](#), [5](#), [9](#)

[46] D. Martin, C. Fowlkes, D. Tal, and J. Malik, "A database of human segmented natural images and its application to evaluating segmentation algorithms and measuring ecological statistics," in *ICCV*, vol. 2. IEEE, 2001, pp. 416–423. [5](#), [6](#)

[47] J.-B. Huang, A. Singh, and N. Ahuja, "Single image super-resolution from transformed self-exemplars," in *CVPR*, 2015, pp. 5197–5206. [5](#), [6](#)

[48] L. Wang, X. Dong, Y. Wang, X. Ying, Z. Lin, W. An, and Y. Guo, "Exploring sparsity in image super-resolution for efficient inference," in *CVPR*, 2021, pp. 4917–4926. [5](#)

[49] X. Luo, Y. Qu, Y. Xie, Y. Zhang, C. Li, and Y. Fu, "Lattice network for lightweight image restoration," *IEEE Transactions on Pattern Analysis and Machine Intelligence*, vol. 45, no. 4, pp. 4826–4842, 2022. [5](#)

[50] G. Gao, Z. Wang, J. Li, W. Li, Y. Yu, and T. Zeng, "Lightweight bimodal network for single-image super-resolution via symmetric cnn and recursive transformer," in *IJCAI*, 2022, pp. 913–919. [5](#), [7](#)

[51] R. Timofte, E. Agustsson, L. Van Gool, M.-H. Yang, and L. Zhang, "Ntire 2017 challenge on single image super-resolution: Methods and results," in *CVPRW*, 2017, pp. 114–125. [6](#)

[52] J. Cai, H. Zeng, H. Yong, Z. Cao, and L. Zhang, "Toward real-world single image super-resolution: A new benchmark and a new model," in *ICCV*, 2019, pp. 3086–3095. [6](#), [7](#)

[53] Z. Wang and A. C. Bovik, "A universal image quality index," *IEEE Signal Processing Letters*, vol. 9, no. 3, pp. 81–84, 2002. [6](#)

[54] R. Zhang, P. Isola, A. A. Efros, E. Shechtman, and O. Wang, "The unreasonable effectiveness of deep features as a perceptual metric," in *CVPR*, 2018, pp. 586–595. [6](#)

[55] T. Yao, Y. Pan, Y. Li, C.-W. Ngo, and T. Mei, "Wave-vit: Unifying wavelet and transformers for visual representation learning," in *ECCV*. Springer, 2022, pp. 328–345. [9](#)

[56] P. Jeevan, A. Srinidhi, P. Prathiba, and A. Sethi, "Wavemixsr: Resource-efficient neural network for image super-resolution," in *WACV*, 2024, pp. 5884–5892. [10](#)